



저작자표시-비영리-변경금지 2.0 대한민국

이용자는 아래의 조건을 따르는 경우에 한하여 자유롭게

- 이 저작물을 복제, 배포, 전송, 전시, 공연 및 방송할 수 있습니다.

다음과 같은 조건을 따라야 합니다:



저작자표시. 귀하는 원저작자를 표시하여야 합니다.



비영리. 귀하는 이 저작물을 영리 목적으로 이용할 수 없습니다.



변경금지. 귀하는 이 저작물을 개작, 변형 또는 가공할 수 없습니다.

- 귀하는, 이 저작물의 재이용이나 배포의 경우, 이 저작물에 적용된 이용허락조건을 명확하게 나타내어야 합니다.
- 저작권자로부터 별도의 허가를 받으면 이러한 조건들은 적용되지 않습니다.

저작권법에 따른 이용자의 권리는 위의 내용에 의하여 영향을 받지 않습니다.

이것은 [이용허락규약\(Legal Code\)](#)을 이해하기 쉽게 요약한 것입니다.

[Disclaimer](#)

Master's Thesis of Science in Agriculture

**Study for Enhancing Knock-in Efficiency and
Inversion-mediated Animal Production using
CRISPR/Cas9**

**CRISPR/Cas9을 통한 녹인 효율 향상과 유전자 역위 동물 생산에
대한 연구**

February 2020

Jeongpil Han

**Department of International Agricultural Technology
Graduate School of International Agricultural Technology
Seoul National University**

Study for enhancing knock-in efficiency and inversion-mediated animal production using CRISPR/Cas9

A thesis
submitted in partial fulfillment of the requirements to the faculty
of Graduate School of International Agricultural Technology
for the Degree of Master of Science in Agriculture

By
Jeongpil Han

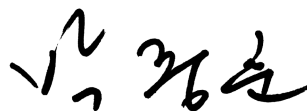
Supervised by
Prof. Su Cheong Yeom

Major of International Agricultural Technology
Department of International Agricultural Technology
Graduate School of International Agricultural Technology
Seoul National University

December 2019

Approved as a qualified thesis
for the Degree of Master of Science in Agriculture
by the committee members

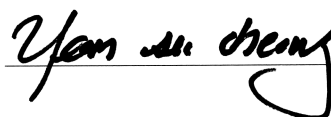
Chairman **Joonghoon Park, Ph.D.**



Member **Tae Sub Park, Ph.D.**



Member **Su Cheong Yeom, Ph.D.**



Abstract

Clustered regularly interspaced short palindromic repeat (CRISPR)/CRISPR associated (Cas) system has been widely applied for genome editing. CRISPR/Cas system occurs error-prone non-homologous end joining (NHEJ) and error-free homology directed repair (HDR) in eukaryotic cells. Increasing efficiency of Knock-in (KI) is exceedingly important in this field, I studied mechanism to increase the efficiency. In addition, due to absence of Hemophilia A (HA) inversion mouse model, I generated novel inversion-mediated hemophilia A mouse model with CRISPR/Cas9.

To enhance KI efficiency that I conducted several experiments; using single strand oligodeoxynucleotides (ssODNs) as a homologous template and in order to evaluate the KI efficiency by electroporation, the transition of RNP complex and ssODN was observed by immunostaining according to cell cycle. I found that single strand template repair (SSTR) efficiency was improved in mitosis, especially at meta- and anaphase, when the nuclear envelope was absent. Cas9 protein with a nucleus localizing signal (NLS) readily migrated into the nucleus, but the ssODN was blocked from nuclear envelope to transport into the nucleus before mitosis. This resulted in NHEJ prior to the arrival of the ssODN. To circumvent problems posed by the nuclear envelope, NLS-tagged ssODNs were assessed. NLS-tagging enhanced over 4-fold SSTR and indel efficiency than the control. To summary, CRISPR/Cas-mediated genome editing would give rise to better results when conducted at mitosis stage. Furthermore, NLS-tagged ssODN as a donor template appears to maximize the KI efficiency.

Discovery of CRISPR/Cas is the starting point for a new era in producing genetic

engineered animal model. Thousands of novel animal models are produced, however there are no previous reports of *FVIII* intron22 inversion(inv22) mouse models for severe Hemophilia A (HA). I induced NHEJ-mediated *FVIII* inv22 to mimic human severe HA with CRISPR/Cas system in mouse embryos. *FVIII* inv22 mice exhibited a severe hemophilia phenotype with loss of FVIII activity, disorder of blood coagulation and high death rate.

In conclusion, these results suggest that mitosis is an optimal phase for SSTR, and the donor template needs to be delivered to the nucleus prior to the nuclease. Additionally, *FVIII* inv22 mouse is a suitable pre-clinical animal model for gene therapy or gene correction studies of HA.

Key words: Cell cycle, CRISPR, Factor VIII, Mitosis, SSTR

Student number: 2018-28522

Contents

Abstract.....	i
Contents.....	iii
List of Tables.....	v
List of Figures.....	vi
List of Abbreviation.....	vii
 Chapter I : Cell cycle and nuclear envelope affect single strand template repair efficiency	
1. Introduction.....	1
2. Materials and Method	3
2.1 Animal and embryo preparation	
2.2 Embryonic whole mount immunostaining for cell cycle determination	
2.3 In silico sgRNA design and homology template preparation	
2.4 Electroporation-mediated ribonucleoprotein transfection into embryos and genotyping	
2.5 Nuclear localizing analysis for Cas9 protein and ssODN	
2.6 Establishing SpCas9 overexpression NIH3T3 cells	
2.7 Preparation of modified ssODN and Cdk1	
2.8 Cell cycle synchronization and transfection of cells by electroporation	
2.9 Targeted deep sequencing	
2.10 Statistical analysis	
3. Result.....	11
3.1 Embryonic cell cycle analysis by nuclear envelope morphology	

3.2 Mitosis-specific high SSTR efficiency	
3.3 The nuclear envelope as a major barrier to the transport of ssODN to the nucleus	
3.4 High SSTR efficiency in mitotic synchronous embryos and cells	
3.5 Minimal impact of ssODN size and Cdk1 on SSTR efficiency	
3.6 Improving SSTR efficiency using NLS tagged ssODN	
4. Discussion.....	24
Chapter II : Novel severe hemophilia A mouse model with Factor VIII intron 22 inversion	
1. Introduction.....	26
2. Materials and Method	27
2.1 sgRNA preparation	
2.2 Mutant generation	
2.3 ELISA and chromogenic assay	
2.4 Histological examination	
2.5 In vivo bleeding test	
2.6 Survival rate analysis	
3. Results.....	30
3.1 Generation of <i>FVIII</i> intron22 inversion mouse model	
3.2 Validation of <i>FVIII</i> intron22 inversion-mediated blood coagulation disorder	
4. Discussion.....	35
5. References.....	36
6. Abstract in Korean.....	39

List of Tables

Table 1. sgRNA sequences used in this study	5
Table 2. ssODN sequences for genotyping used in this study	6
Table 3. Primer sequences for genotyping used in this study	8

List of Figures

Figure 1. Identification of embryonic cell cycle and correlation with NHEJ and SSTR.....	14
Figure 2. Nucleus localization analysis of RNP and ssODN.....	16
Figure 3. Physical barrier around condensate chromosome in mitosis.....	17
Figure 4. G1 and mitosis dependent NHEJ and SSTR analysis.....	19
Figure 5. Analyzing NHEJ and SSTR efficiency with ssODN size and NLS conjugation.....	22
Figure 6. Generation of Factor VIII intron 22 inversion (<i>FVIII</i> inv22) mouse	31
Figure 7. Hemophilia phenotyping with <i>FVIII</i> inv22 mice.....	34

List of Abbreviations

AAV	Adeno associated virus
B6	C57BL/6
Cas9	CRISPR associated protein9
CRISPR	Clustered regularly interspaced short palindromic repeats
DSB	Double Strand Break
dsDNA	double strand DNA
FA	Fanconi anemia
HA	Hemophilia A
hCG	human Chorionic Gonadotropin
HDR	Homology directed repair
HR	Homologous Recombination
IU	International Unit
KI	Knock In
mRNA	messenger RNA
NHEJ	Non-homologous end joining
NLS	Nucleus localizing sequence(signal)
MEF	Mouse embryonic fibroblast
nt	nucleotide
PAM	Protospacer adjacent motif
PCR	Polymerase chain reaction

PMSG	Pregnant mare's serum gonadotropin
PN	Pronucleus
RNP	Ribonucleoprotein
sgRNA	single guide RNA
SpCas9	Streptococcus pyogenes Cas9
ssODN	single-stranded oligodeoxynucleotide
SSTR	Single Stranded Template Repair
T7E1	T7 Endonuclease I
WT	Wild Type

Chapter I

**Cell cycle and nuclear envelope
affect single strand template repair
efficiency**

1. Introduction

Eukaryotic cells have two DNA repair systems, namely error-prone non-homologous end joining (NHEJ) and error-free homologous recombination (HR). Although HR has been traditionally used for gene targeting in embryonic stem cells, random genetic damage due to electroporation results in a low specificity and efficiency. Recently developed nucleases are able to recognize specific sequences and create double strand breaks (DSBs). Zinc finger nuclease and transcriptional activator-like effector nuclease are able to recognize specific sequences, but do not have the ability to create DSBs without conjugating to *ForkI*. On the contrary, clustered regularly interspaced short palindromic repeat (CRISPR)/CRISPR associated (Cas) nucleases can be used to recognize complementary sequences and induce DSBs by themselves. These nucleases are widely utilized for gene manipulation using NHEJ or homology directed repair (HDR) [1].

For small sequence knock-in (KI) or nucleotide substitution, single strand oligodeoxynucleotide (ssODN) is usually used as a template, a method known as single strand template repair (SSTR). Classical HR is a Rad51-dependent pathway and uses double stranded DNA (dsDNA) as a template, while SSTR is a Rad51-independent and Fanconi anemia (FA) DNA repair pathway [2]. Although SSTR has been shown to exhibit a relatively higher KI rate than does HR, there were still many studies for improving efficiency such as those on the 3'-end phosphorothioate or methyl-CpG modification of ssODN [3, 4], HR promoting or NHEJ-blocking small molecules [5], and the use of overlapping sgRNAs [6]. Previous studies have mainly focused on the control of DSBs size, ssODN stability, and the control of the DNA repair cycle, and there is a lack of research on the correlation between the cell cycle and SSTR efficiency.

Although the cell cycle plays an important role in the selection of the NHEJ or HR repair pathways after DNA damage, error-free HR mainly occurs at the S/G2 phase [7, 8]. Even though SSTR has different mechanisms than HR [2], the mechanism for SSTR efficiency is still unknown, and the cell cycle is increasingly drawing attention as a potential regulator. Recent studies have reported a high SSTR efficiency at the G2/M stage [9, 10]. However, this is different from our expectations, wherein an error-free repair would occur at the G2/S

phase. Even though the cell cycle seems to be related to SSTR efficiency, the use of cells to analyze the cell cycle has limitations due to the difficulty of distinguishing the changes in the nuclear DNA. To confirm the correlation between the cell cycle and SSTR efficiency, mouse embryos have several advantages over cells for the analysis of the cell cycle, including easy synchronization with scheduled superovulation and a relatively large nucleus.

In this study, I investigated the correlation between the cell cycle and SSTR efficiency using mouse embryos. After defining the embryonic cell cycle, mouse embryos were used in Cas9 ribonucleoprotein (RNP) and ssODN electroporation studies. The mechanism of the change in SSTR efficiency during the cell cycle was confirmed, and based on this, a method to improve SSTR efficiency was presented.

2. Materials and Method

2.1 Animal and embryo preparation

C57BL/6 mice were obtained from Koatech (PyeongTaek, Korea) and maintained under specific pathogen free conditions. For estrus synchronization and superovulation, pregnant females were injected with 5 IU of serum gonadotropin (Prospec Bio, East Brunswick, USA) and 5 IU of human chorionic gonadotropin (hCG) (Prospec) at 48 h intervals. The females were then mated with the sperm donor mice. Hormone injections and mating were performed at 2 pm to synchronize the cell cycle of the embryo. Embryos were collected from the oviducts. Embryos with a normal shape with pronuclei were cultured in KSOM medium (Merck Millipore, Billerica, MA, USA). This study was approved by the Institutional Animal Care and Use Committees of Seoul National University (SNU-180315-4, SNU-1708164, and SNU-180827-4) and was conducted in accordance with approved guidelines.

2.2 Embryonic whole mount immunostaining for cell cycle determination

The embryos were randomly divided into five groups. Whole mount immunofluorescence of Lamin A/C and Lamin B was performed 24 (2 pm), 26 (4 pm), 28 (6 pm), 30 (8 pm), and 32 h (10 pm) after hCG injection, respectively. Briefly, the embryos were fixed in 4% paraformaldehyde in PBS for 30 min, followed by washing 4 times in 0.01% bovine serum albumin in PBS (BSA-PBS), permeabilization with 0.5% Triton X in PBS for 30 min, and blocking with 3% BSA-PBS. Next, the embryos were incubated with the primary antibodies Lamin A/C Alexa 594 (red fluorescence and clone: E-1) (Santa Cruz Biotechnology, Dallas, TX, USA) and Lamin B Alexa 488 (green fluorescence and clone: B-10) (Santa Cruz) overnight at 4°C. The following day, the embryos were mounted on slides using DAPI containing mounting gel (ProLong Gold antifade reagent; Invitrogen, Carlsbad, CA, USA),. Fluorescence was detected using a confocal microscope (Leica TCS SP8; Leica, Germany) the next day.

2.3 In silico sgRNA design and homology template preparation

sgRNAs were designed with a 20 nt binding sequence to target the *Rosa26* locus, *Haptoglobin* (*Hp*), *Factor VIII* intron 22 (*F8 int22*), and a 219 kb distance intragenic region (*F8* distal). They were synthesized using an *in vitro* RNA synthesis kit (Thermo Fisher

Scientific, Waltham, MA, USA) after PCR amplification. The sgRNA of each target region was designed with overlapping binding sites [6]. A 200 nt ssODN with 60–75 nt homology sequences was also prepared (Integrated DNA Technologies, Skokie, IL, USA). The sgRNA and ssODN sequences are provided in (Table 1 and 2).

2.4 Electroporation-mediated ribonucleoprotein transfection into embryos and genotyping

Electroporation was performed to transfer the Cas9 RNP and ssODN into the embryos at the five time points under the previously reported conditions [11]. Briefly, the embryos were washed 3 times with Opti MEM I medium (Invitrogen, Carlsbad, CA, USA). Then, approximately 50 embryos were transferred into the electroporation buffer on the electrode. The final concentration of the electroporation buffer consisted of 200 ng/ μ L of *Streptococcus pyogenes* Cas9 protein (SpCas9) (Toolgen Inc, Seoul, Korea), 50 ng/ μ L of each sgRNA, and 100 μ mole of ssODN. The electroporation pulse conditions were as follows: 7 cycles of 30 V with 3 ms ON and 97 ms OFF. After washing with M2 medium (MTI-GlobalStem, Rockville, MD, USA), the embryos were transferred into the KSOM medium (Merck Millipore, St. Louis, MO, USA) until embryo transfer into the recipient donor or blastocyst stage for genotyping. For blastocyst genotyping, single embryos were transferred to 10 μ L of distilled water and used as the PCR template after performing three freeze-thaw cycle and incubating at 95 °C for 15 min. Next, the PCR amplicons were subjected to an additional T7E1 assay (NEB, Ipswich, MA, USA). All primers used for genotyping are listed in (Table 3).

2.5 Nuclear localizing analysis for Cas9 protein and ssODN

A one hundred-nucleotide-sized ssODN was synthesized with a Cy-3 peptide conjugation at the 5' end (Bioneer, Daejeon, Korea). The embryos were randomly divided into two groups, followed by electroporation with hemagglutinin (HA)-conjugated SpCas9 RNP with Rosa26 targeting sgRNAs and Cy3-conjugated ssODN 25 h (3:00 pm) and 29 h (7:00 pm) after hCG injection. Half of the embryos were immediately fixed with 4% paraformaldehyde in PBS for 30 min, and the remaining embryos were fixed after 2 h. Embryo whole mount immunostaining was performed using anti-HA Alexa 488, to detect RNP (green fluorescence), and DAPI. Fluorescence was observed using a confocal microscope (Leica), and the localization of the green and red signals was analyzed (Figure 2a).

Table 1. sgRNA sequences used in this study

Target gene		sgRNA binding sequence	PAM
<i>Rosa26</i>	sgRNA 1	GACTGGAGTTGCAGATCACG	AGG
	sgRNA 2	GCAGATCACGAGGGAAGAGG	GGG
<i>Hp</i>	sgRNA 1	CCAATGATGGCCACAGTCAT	AGG
	sgRNA 2	GATGGCCACAGTCATAGGTT	AGG
<i>FVIII int22</i>	sgRNA1	TTACTAAGGGCTGAACAAGG	AGG
	sgRNA2	GACTTACTAAGGGCTGAACA	AGG
<i>FVIII distal</i>	sgRNA1	GCATACGGGTCAGATGCCTG	GGG
	sgRNA2	CCAAATACGGCAGGGCATAAC	GGG
<i>Target1</i>	sgRNA1	CAGGGTTTTCAGCTCCTAAC	TGG
	sgRNA2	TGGGGCGGAGGATCCAGTT	AGG
<i>Target2</i>	sgRNA1	CACTGGGAGGTTATCACTGG	TGG
	sgRNA2	AGTCCGACGCACGCACTGGG	AGG

Table 2. ssODN sequences for genotyping used in this study

Target gene	sgRNA binding sequence
<i>Rosa26</i>	GGACCGCCCTGGGCCTGGGAGAAATCCCTTCCCCCTCTTCCCTCGTATAACTTCGTATAATGTATGCTATACGAAAG TTATTTTCGAATTCTGCAGTCGACGGTACCGCGGGCCCGGATCCATATAAATTCGTATAGGATACTTTTATACGAA GTTATGATCTGCAACTCCAGTCTTTCTAGAAGATGGCGGGAGTCTTCTG
<i>Hp</i>	AGCATTTAAGTGTGCTGTGTACCAATGATGGCCACAGTAGTATCTACATTTTATTACCACATCTTTTGCGGT GTCTGAGGGAGGTTTCTCTTTCTGGAGGGCTCTGTATATTTGCCAATGTACTTTCTGAAATGCAGCCAGAA ACTGAGCCCAACCCATAGGTAGGAAGACAGACAGTTTCTGGCATCTTGGG
<i>FVIII int22</i>	GTTCTGCAAAATGAAGAACTCTGGACTTACTAAGGGCTGATAAATTCGTATAGCATACATTATACGAAGTTAT TTCGAAATCTGCAGTCGACGGTACCGGGCATCTGGGGACGGCAGAGGTATCACACGGCTGAACGTTACCAG CACCCCGAGAACACAAAGGAGGTACTTGTGTGTAAGTGGGGAACAATGCTA
<i>FVIII distal</i>	TGCCCTGCTTCTGCTTAAAGCCTTTCATCCCCAGGCATCTGGGGACGGCAGGGTATCACACGGC TGAAACGTTACCAAGCACCCCGAGAACACTTCGAATTCGCAATCGACGGTACCCGATAAATTCGTATAATGTATG CTATACGAAAGTTATACCCGTATGCCCTGCCGTATTTGGTTGTGCCAGCACCTCT
<i>Rosa26-NLS</i>	GAATCCCTTCCCCCTCTTCCCTCGTAATGCGTACCGATCTGCAACTCCAGTCTTTTCTAGA
<i>Rosa26-60nt</i>	TGGGAGAAATCCCTTCCCCCTCTTCCCTCGTGGATTATTCATACCGTCCCAGATCTGCAACTCCAGTCTTTCTAGA AGATG
<i>Rosa26-120nt</i>	TCTGAGGACCGCCCTGGGCCTGGGAGAAATCCCTTCCCCCTCTTCCCTCGTGGATTATTCATACCGTCCCAGATC TGCAACTCCAGTCTTTCTAGAAAGATGGCGGGAGTCTTCTGGGCAG
<i>Rosa26-160nt</i>	TTCTCTGCTGCCTCTTGCTTCTGAGGACCGCCCTGGGCCTGGGAGAAATCCCTTCCCCCTCTTCCCTCGTGA

	TTATTATACCGTCCCAGATCTGCAAACTCCAGTCTTTCTAGAAAGATGGCGGGA GTCTTCTGGGCAGGCTTAA AGGCTAACCTGGTG
<i>Rosa26-200nt</i>	TTGCAATACCTTTCTGGGAGTTCTCTGTGCTCCTCGCTTCTGAGGACCGCCCTGGGCCCTGGGAGAAATCCCT TCCCCCTCTTCCCTCGTGGATTATTCATACCGTCCAGATCTGCAACTCCAGTCTTTCTAGAAAGATGGCGGGA GTCTTCTGGGCAGGCTTAAAGGCTAACCTGTGTGTGGCGGTTGTCTCTGCAGG
<i>Target1</i>	CCCTGACCCCCGAAAGCTAAGGAAACCTGGTTTCCACGCCACTAACACCTTCTCTTGTCCAGCAGGGTTTT CAGTCCGTGAGCGGCTGGCGGCTGTTCAAGAAAGATTAGCTAACTGGATCCTCCGCCCCCATGGGATATGGGG TGGCTGCCCTGAGTGCCCAACGCCGAGGGCGCGCAAGTTGACTAAAC
<i>Target2</i>	CCCTCTCCAGCTCTTCCATCTCCTCCACGTCCTTCCCACCGTCCTATGACAGCGTCACGAGGGCCACCAGTGAT AACCTCCCAGTGCGTGCCTCGGACTACAGCCGCAGCGAAGATCTTGCAGACTTCCCTCCCATCTCCAGATAGGG ACCGAGAGTCTAT

Red alphabet : KI sequence

Table 3. Primer sequences for genotyping used in this study

Target gene	Primer	Product size (bp)	Annealing Tm. (°C)
<i>Rosa26</i>	F: 5'-TGATGTAAGAAGGGGAGTGG-3'	693	60
	R: 5'-AGGAGGAGAGAAAGGATGC-3'		
<i>Hp</i>	F: 5'-AGAAGGGCCAAATCACAG-3'	759	60
	R: 5'-AGGAGAGAGGAGGTGGAAAG-3'		
<i>FVIII int22</i>	F: 5'-TGGCGGAGGAGGTGAAAA-3'	848	59
	R: 5'-AGAGGGGGCTGAAGAAAAAGA-3'		
<i>FVIII distal</i>	F: 5'-GGCACAAACCAATACGGCA-3'	762	59
	R: 5'-GCCCCCTCCATAAGCATTTCA-3'		
<i>Target1</i>	F: 5'-TGGAGAGTTAGGGGCAGT-3'	423	61
	R: 5'-GGTTGGGGTTGAGAGAAAG-3'		
<i>Target2</i>	F: 5'-GCATGCTTCCTCCCTCTT-3'	212	60
	R: 5'-CACGCACCTGTCGGTTAT-3'		

2.6 Establishing SpCas9 overexpression NIH3T3 cells

To establish SpCas9 overexpression (NIH3T3-SpCas9) cells, 3 µg of pITR-CAG-SpCas9(RF)-ITR and pPiggyBac transpose were co-transfected into 6×10^5 NIH3T3 cells (ATCC CRL-1658; American Type Culture Collection, VA, USA). Three days after transfection, high RFP-expressing cells were sorted using flow cytometry.

2.7 Preparation of modified ssODN and Cdk1

For the preparation of NLS-tagged ssODN, 60-nucleotide-sized ssODNs with 25 nt homology and 10 nt KI sequence were synthesized. Half of these were then tagged with a SV40-derived nucleus localizing signal peptide (Pro-Lys-Lys-Lys-Arg-Lys-Val-Cys) by synthesis (Genscript, Piscataway, NJ, USA). In addition, ssODNs of different sizes were designed and synthesized as 20 nt of a KI sequence with 30, 50, 70, and 90 nt homologous sequences (Integrated DNA Technologies, Coralville, IA, USA). The sequences of each ssODN are provided in (Table 2). In the Cdk1 treatment experiments, the Cdk1 (Sigma, St. Louis, MO, USA) concentrations provided differently under the same RNP and sgRNA conditions.

2.8 Cell cycle synchronization and transfection of cells by electroporation

The NIH3T3-SpCas9 cell line was cultured in DMEM and 10% FBS. To synchronize the G1 and G2/M stages, 2 mM of hydroxyurea (Sigma) and 200 ng/mL nocodazole (Sigma) were added to 1×10^6 of cells [9]. The cell cycle was then analyzed using 7-aminoactinomycin D (7-AAD) stain and flow cytometry analysis (BD Bioscience, San Jose, CA, USA). Next, transfection into 2×10^5 NIH3T3-SpCas9 was performed using a Neon electroporator (Thermo Fischer Scientific, Waltham, MA, USA) with a mixture containing 1 µg of Rosa26 locus-targeting sgRNA and 100 µ mole ssODN. Cell harvesting and gDNA extraction was performed 72 h after transfection, followed by deep sequencing.

2.9 Targeted deep sequencing

After performing PCR using Phusion Taq polymerase (New England Biolabs, MA, USA), the PCR amplicons were subjected to paired-end deep sequencing using Mi-seq (Illumina, San Diego, CA, USA). The deep sequencing data were analyzed using Cas-Analyzer (www.rgenome.net)[12]. An indel appearing 3 bp upstream of the '5-NGG-3' PAM was

considered as a mutation caused by RNP and KI efficiency was calculated with matching between read sequence and reference sequence.

2.10 Statistical analysis

Statistical analysis was performed using unpaired Student's *t*-test with GraphPad Prism (GraphPad, San Diego, CA, USA). Significance was defined as $p < 0.05$.

3. Result

3.1 Embryonic cell cycle analysis by nuclear envelope morphology

Embryo development and its characteristics have been studied extensively [13], however, there is currently a lack of reports that define the cell cycle phases of early stage embryos. Thus, I sought to identify the cell cycle of early stage embryos at different times after hCG treatment. After estrus synchronization and superovulation, female mice were mated with sperm donor mice at 2 pm. The resulting embryos were collected at 10 am the next day. Since two-cell embryos develop at around 8 pm (30 h after hCG injection), embryonic cell cycle analysis was performed between 2 and 10 pm. The eukaryotic cell cycle consists of Gap 1 (G1), Synthesis (S), Gap 2 (G2), and Mitosis, however, early embryos progress in the following order: pronuclear formation (PN 0~5), mitosis, and G1 at the early two-cell stage [14]. When the PN stage is further subdivided, P1 to early P3 are classified as the G1 phase, late P3 to PN4 as the S phase, and PN5 as G2 [15]. The embryonic cell cycle is defined by the presence of a nuclear membrane, chromosome condensation, and DNA synthesis [16]. Approximately 24 h after hCG injection (2 pm), the embryos were found in PN2, and a Lamin A/C and Lamin B positive nuclear envelope began to appear. Between 28 and 30 h after hCG injection (6–8 pm), half of the embryos were found in the mitotic phase with chromatin condensation and loss of the nuclear envelope following cytokinesis and differentiation. Although the duration of mitosis was unclear, it appeared to last for about 2 h (Figure 1a). The frequency of the mitotic embryo gradually increased until 6 pm (28 h after hCG injection), and about half of the embryos were found in mitotic phase between 6 pm and 8 pm. G1 two-cell embryos were the predominant type at 10 pm (Figure 1b). The embryonic cell cycle at each time point was similar to that reported by a previous study [14].

3.2 Mitosis-specific high SSTR efficiency

After confirming the embryonic cell cycle by time point, four different target genes were used to investigate the correlation between the cell cycle and SSTR efficiency. First, one or two time points were selected in PN, mitosis, and G1 phase, and 110 to 120 bp KI SSTR experiments were performed using the mouse embryos (Figure 1c). In electroporation with RNP and ssODN, the overall morula or blastocyst stage development incidence increased

with time, presumably due to the increased stability of the embryo (Figure 1d). T7E1 analysis indicated that the incidence of indel formation was approximately 80% in the PN and M phases, although, this decreased in the G1 phase of Rosa26 targeting (Figure 1e). Interestingly, SSTR efficiency appeared to be correlated with the cell cycle, with a low overall SSTR efficiency in PN2~PN5 phase, which increased to 20~50% at mitosis, before decreasing again at G1 of the two-cell phase. However, the SSTR efficiency in PN1 (20 h after hCG injection, 10 pm) was high for *R26* and *Hp*, but was less consistent for F8-related target genes. Nevertheless, this suggests a high SSTR efficiency in mitosis, a pattern that was repeated in all of the four different targets (Figure 1f).

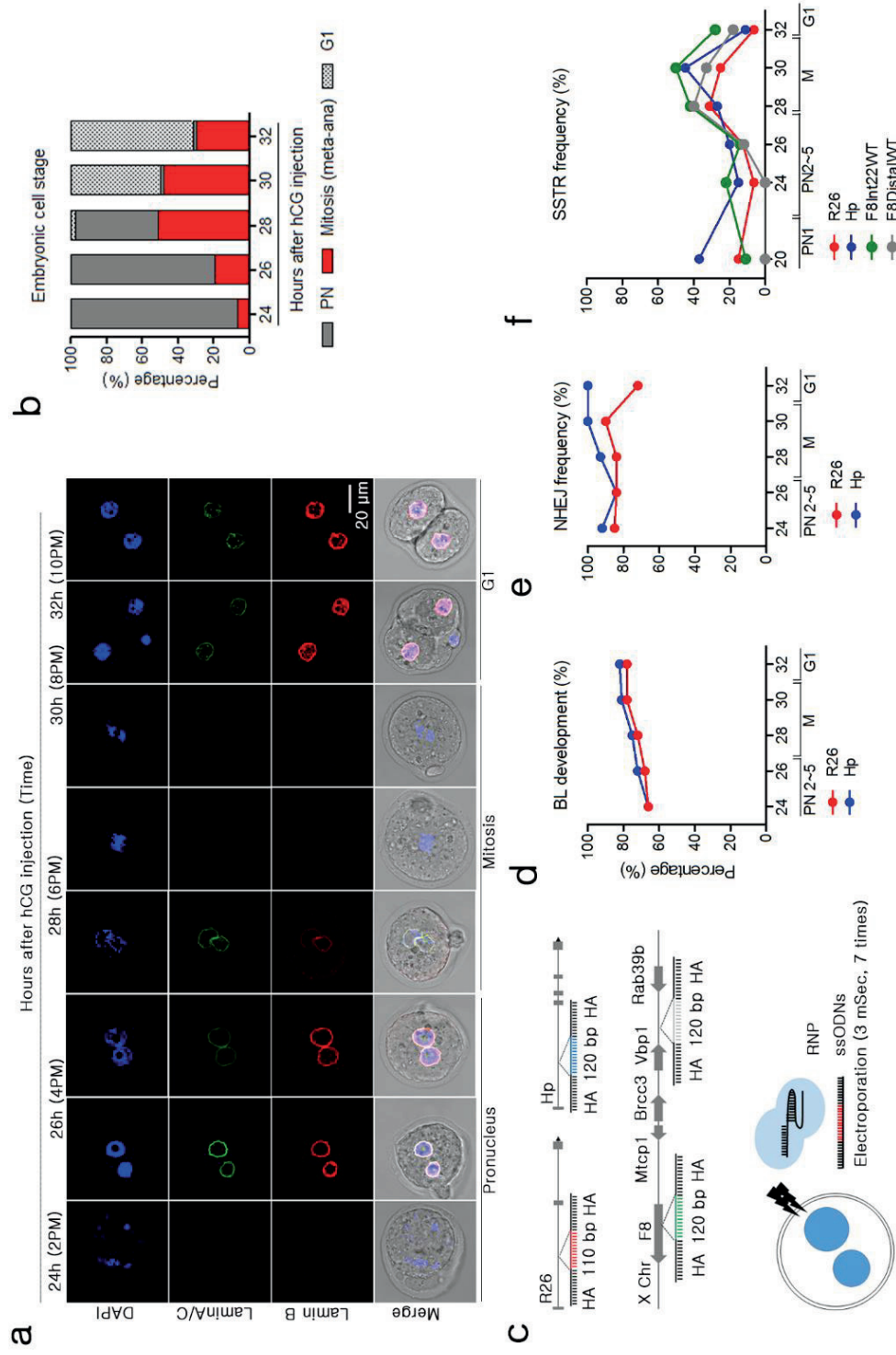


Figure 1. Identification of embryonic cell cycle and correlation with NHEJ and SSTR. **a)** For whole mount staining of the nuclei (DAPI) (blue), Lamin B (green), and Lamin A/C (red), randomly divided embryos were used for immune staining at 2, 4, 6, 8, and 10 pm. Fluorescence was detected using a confocal microscope. The embryonic cell stage was defined based on the presence of a nuclear envelope, nucleus condensation, and embryonic division. A representative image is shown for each time. **b)** The embryonic cell stage was defined, and the frequency was calculated. Embryos with 2 PN designated the presence of PN, embryos with condensing nuclei and without a nuclear membrane were in mitosis, and two-cell embryos were calculated as being found in G1. **c)** Schematic representation of small sequence insertion by ssODN into 4 different targets (*Rosa26*, *Hp*, *F8* intron 22, and intragenic site between *Vbp1* and *Rab39b*). For small sequence insertions of 110–120 bp into the target site, 2 binding site-overlapping sgRNAs and ssODNs with 40–45 homology sequences were applied. **d)** The toxicity of electroporation was evaluated by calculating blastocyst development (% of blastocyst per total embryos) after electroporation with ssODN template and RNP. **e)** NHEJ frequency was calculated by PCR and T7E1 analysis after SpCas9 RNP electroporation at each time period. **f)** The presence of SSTR was analyzed by PCR, and the frequency was calculated as the % of KI embryos per total embryos.

3.3 The nuclear envelope as a major barrier to the transport of ssODN to the nucleus

The most prominent feature of the mitotic phase is chromosome condensation and the loss of the nuclear envelope. Mitosis is divided into prophase, prometaphase, metaphase, anaphase, and telophase. Loss of the nuclear envelope was observed between metaphase and anaphase. Since chromosomal condensation was expected to inhibit the access of RNP and ssODN to the target sequence, I focused on the correlation between the nuclear envelope and SSTR efficiency. The cell cycle was found to have a high indel frequency but varying SSTR efficiencies (Figure 1e and 1f), suggesting that there were different efficiencies of transnuclear RNP and ssODN transport. To confirm this hypothesis, I prepared a 5'-Cy3 conjugated 100-nucleotide (nt) ssODN and a Rosa26 locus-specific RNP, of which SpCas9 protein conjugate hemagglutinin and NLS. This allowed us to analyze the localization of ssODN and RNP using fluorescence detection (Figure 2a). Electroporation was performed using PN phase and M phase embryos, taking into consideration the presence of a nuclear membrane and the transport. Half of the embryos were fixed immediately, and the remaining half were fixed after 2 h in order to analyze changes over time. In the PN phase (25 h after hCG injection, 3 pm), only RNP crossed the nuclear envelope (green spots in the nucleus).

Even at 2 h post-electroporation (27 h after hCG injection, 5 pm), more RNP was found than ssODN. On the other hand, both RNP and ssODN were diffusely distributed throughout the embryo, as there was no nuclear membrane at the mitotic stage (29 h after hCG injection, 7 pm). This result suggests that NHEJ, but not SSTR, is predominantly found in the embryos, particularly in the PN phase, owing to the lack of ssODN as a homology template during DNA cleavage by RNP (Figure 2b). Furthermore, this indicates why some target genes showed a high SSTR efficiency in the PN1 phase (20 h after hCG injection, 10 am), as the nuclear envelope had not fully developed.

The localization analysis of RNP-ssODN also resulted in several interesting findings. Firstly, there appeared to be an immediate penetration of RNP via an active nuclear envelope transport system using tagged NLS signals (Figure 2b). Secondly, most of the ssODN and RNP were distributed in the cytosol rather than the nucleus, suggesting that using high doses of RNP and ssODN is inefficient for electroporation. Thirdly, even though the structural nuclear envelope disappears during mitosis, there appear to be additional physical barriers outside the chromosome that restrict access to RNP and ssODN (Figure 3).

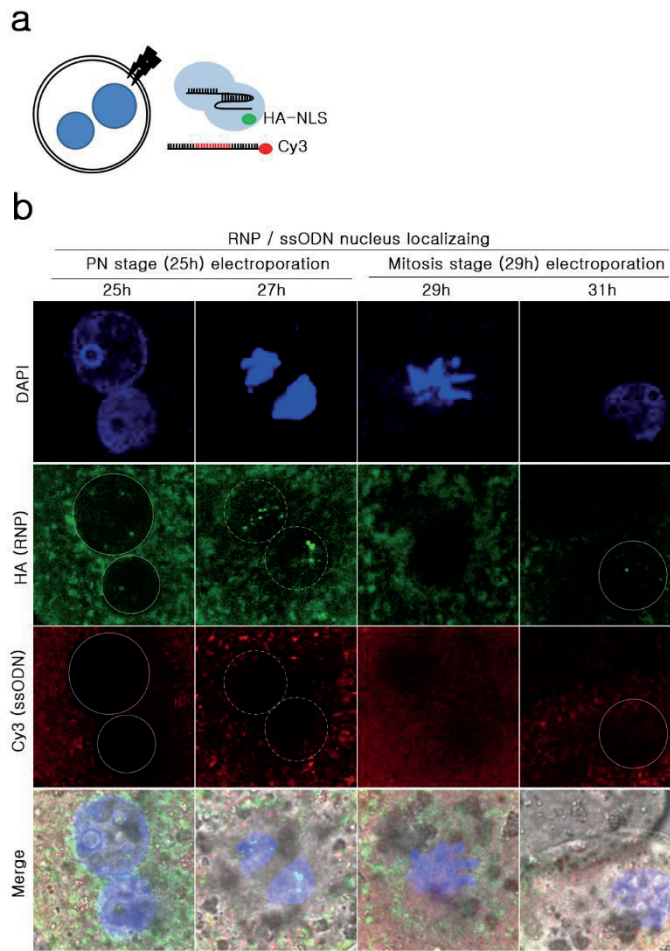


Figure 2. Nucleus localization analysis of RNP and ssODN. **a)** Experimental design. **b)** RNP (HA conjugated SpCas9 and R26 targeting sgRNAs) and Cy-3 conjugated 100 nt-sized ssODN were electroporated into embryos at 3 pm and 7 pm. Next, half were immune stained with HA-Alexa 488 (green) mAb, and the other half were stained after 2 h with the same target. The selected image is shown. White dotted line: disappeared nuclear membrane.

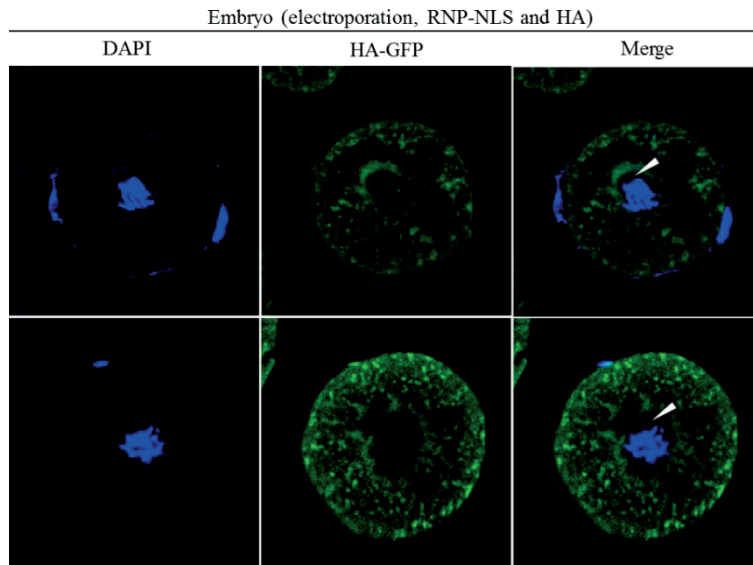


Figure3. Physical barrier around condensate chromosome in mitosis. RNP(HA conjugated SpCas9 and Rs26 targeting sgRNAs) were electroporated into embryos at 7pm. Embryos were immune stained with HA-Alexa 488 (green) and DAPI (blue).

3.4 High SSTR efficiency in mitotic synchronous embryos and cells

In order to verify the reproducibility of high SSTR efficiency in mitosis, I generated mutant mice with a 33 bp insertion before the stop codon and a nucleotide substitution (4-base alteration). A simple comparison of KI animal production efficiency in PN and mitosis was conducted using electroporation at different time points: 25 h after hCG injection (3 pm, PN) and 29 h after hCG injection (7 pm, mitosis) (Figure 4a). PN phase electroporation showed a high SSTR efficiency of 33% and 37%, however, mitotic electroporation developed an approximately 20% higher SSTR rate of 55% and 50% KI mice production at each target (Figure 4b and 4c). Next, I used cells to confirm the high SSTR efficiency in mitosis. Based on previous reports of cell cycle synchronization, I selected nocodazole to block the G2/M phase and hydroxyurea to block G1/S[9] (Figure 4d). In deep sequencing-based analysis, the nocodazole treatment group showed significantly higher NHEJ and KI rates than the hydroxyurea treatment group (Figure 4e). In other words, the G2/M phase provided better conditions than G1 for the transport of the RNP and ssODN templates to the nucleus. In brief, M phase appeared to represent the optimal time for HDR development in cells, given the results of HDR in embryos.

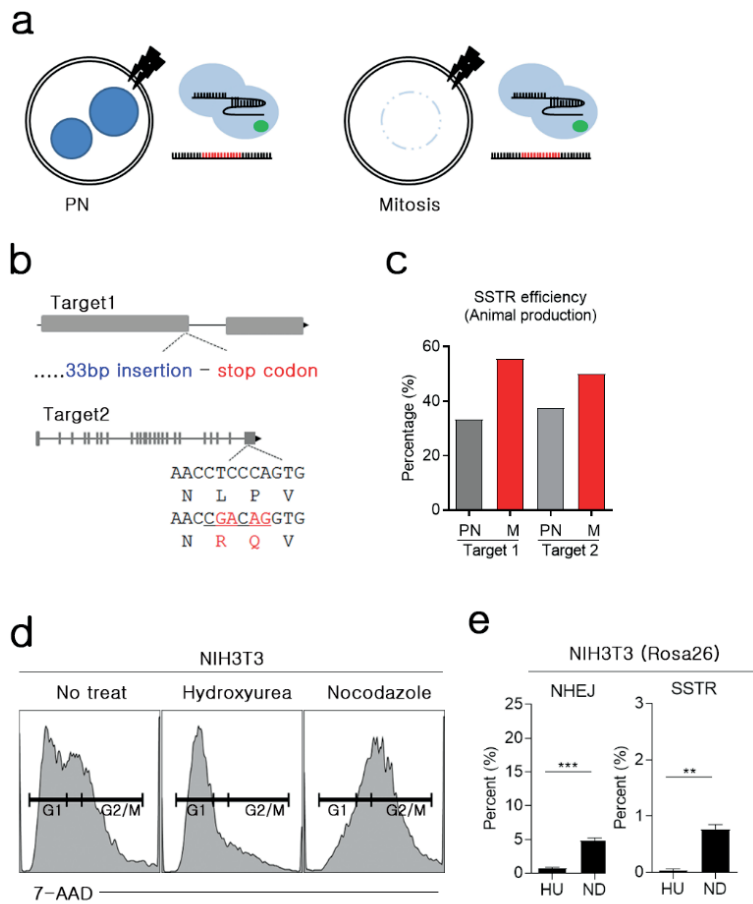


Figure 4. G1 and mitosis dependent NHEJ and SSTR analysis. **a)** Experimental design for cell cycle dependent RNP and ssODN delivery for NHEJ and SSTR. **b)** SSTR strategy for 33 bp insertion before stop codon and nucleotide alteration using SpCas9 RNP and ssODNs. **c)** SSTR efficiency was calculated (% of KI pups per total produced pups). Grey bar: electroporation at PN (3 pm, 25 h after hCG injection). Red bar: electroporation at mitosis (7 pm, 29 h after hCG injection). **d)** Confirming cell cycle synchronization using flow cytometry of hydroxyurea- and nocodazole-treated cells. Anti-7-AAD was used for detection. **e)** The efficiency of NHEJ and SSTR was calculated using deep sequencing after cell cycle synchronization with hydroxyurea (HU, G1) and nocodazole (ND, G2/M) (% of NHEJ or KI reads / total reads). **: $p < 0.01$, ***: $p < 0.001$.

3.5 Minimal impact of ssODN size and Cdk1 on SSTR efficiency

Cell cycle synchronization and cell cycle-specific gene editing are the simplest approaches for high HDR. However, due to the potential limitations of chemical-mediated cell cycle synchronization, including erythrocyte toxicity by nocodazole[17], further experiments were conducted to develop efficient transport methods circumventing the nuclear envelope. Except for mitosis, mRNA and protein can be transported through the nuclear pore in an energy-dependent manner. DNA, on the other hand, is transported to the nucleus via uptake[18]. As such, I first assessed the possibility of transport mediated by diffusion or uptake using different sized ssODNs between 80 and 200 nt (Figure 5a). Nocodazole-treated cell (G2/M) still developed significantly higher NHEJ rate than hydroxyurea-treated cells, and the smaller ssODNs exhibited higher NHEJ rates than the larger ssODNs in both the nocodazole- and hydroxyurea-treated cells (Figure 5b). However, the overall SSTR efficiency was similar between all the cells treated with ssODNs of different sizes (Figure 5c). A longer homology sequence in the large ssODNs resulted in a similar SSTR efficiency while simultaneously overcoming the low NHEJ rate[19]. After confirming that ssODN size does not affect SSTR efficiency, I studied the physical changes of the nuclear envelope and the utilization of the nuclear pore complex (NPC). As Cdk1 and cyclin B control the disassembly of nuclear envelope in mitosis[20], I compared the NHEJ and SSTR efficiency of G1 synchronized NIH3T3 cells after Cdk1 treatment (Figure 5d). The results of the Cdk1 treatment (0, 25, and 50 ng/ μ L) confirmed a dose-dependent increase in NHEJ frequency; however, this difference was not confirmed for SSTR (Figure 5e and 5f). This result suggests that Cdk1 mediates nuclear envelope disassembly and RNP transport but is not sufficient to improve SSTR efficiency.

3.6 Improving SSTR efficiency using NLS tagged ssODN

Next, I used NLS to tag the ssODNs and study the use of energy dependent transportation (Figure 5g). NLS-tagged ssODNs increased the NHEJ rates in both the hydroxyurea and nocodazole groups (Figure 5h), which differed from our expectations. Since RNP was already associated with the NLS signal itself, the NHEJ rates were predicted to occur at a similar rate in all the groups. However, NLS-tagged ssODNs appeared to promote the nuclear transport of RNP. In the analysis of SSTR efficiency, nocodazole treatment also increased the SSTR rate, as expected (Figure 4e and 5i). Notably, NLS tagging with ssODN

increased the SSTR rate by over 4-fold compared to the control in the nocodazole-treated cells (Figure 5i). Taken together, NLS-tagged ssODNs improved the rate of RNP delivery throughout the cell cycle and increased SSTR efficiency, especially during mitosis.

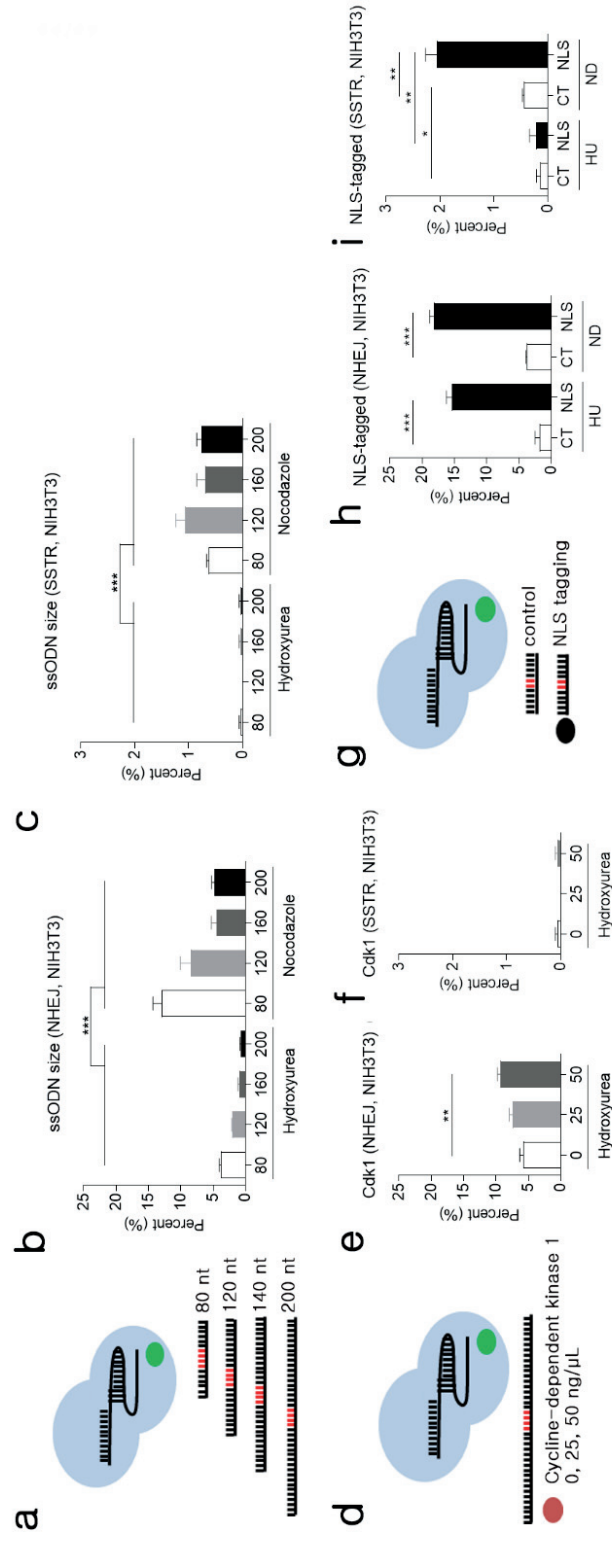


Figure 5. Analyzing NHEJ and SSTR efficiency with ssODN size and NLS conjugation. **a)** Experimental design of different-sized ssODNs. Red region: 20 bp KI sequence. Black region: homology sequence. **b and c)** NHEJ and SSTR frequency were calculated using deep sequencing after cell cycle synchronization and electroporation with 4 different-sized ssODNs (% of NHEJ or KI reads / total reads). **d)** Strategy for Cdk1 treatment. **e and f)** NHEJ and SSTR frequency according to Cdk1 treatment. **g)** Brief schematics for NLS-ssODN conjugation. **h and i)** NHEJ

and SSTR frequency on ssODN and NLS-ssODN donor. Statistical analysis was performed using Student's *t*-test. *: $p < 0.05$, **: $p < 0.01$ and ***: $p < 0.001$

4. Discussion

Since the discovery of CRISPR/Cas9, genetic editing has been used in a variety of fields via loss of function by NHEJ and gain of function by HDR[21]. Gene editing efficiency is particularly important for cell therapy and *in vivo* gene correction, and various methods for enhancing HDR efficiency have been studied. This study demonstrated that the cell cycle plays an important role in HDR efficiency, especially in the restriction of the transport of DNA templates by the NPC, and NLS could be applicable for enhancing NHEJ and SSTR efficiency.

Previous reports have used mouse embryos to study the cell cycle[14, 16]. Here, to analyze the gene editing efficiency according to the cell cycle, I defined the embryonic cell cycle at each time point using *in vivo* fertilized embryos and morphological analysis of the nuclear membrane. Using *in vivo* fertilized embryos, a heterogenous cell phase population was found at each time point, but during mitosis, especially metaphase or anaphase, a higher SSTR efficiency was found, which was caused by the presence of nuclear envelop. The FA DNA repair pathway is the DNA repair mechanism for SSTR[2]. It is activated by inter-strand crosslinks that occur at S phase[22], and maintains chromosomal stability through DNA repair from G2 to M[23]. Even FANCM, as one of the main components of FA and an important player in SSTR, is hyper-phosphorylated in mitosis[2, 24], but the effect of FA on high SSTR in mitosis has not been identified in this study.

A high indel formation potential was found in SpCas9 RNP. As such, to increase the SSTR efficiency, it is necessary to simultaneously deliver the RNP and DNA templates to the target site. In general, the NLS sequences are fused to SpCas9 to facilitate their transfer into the nucleus. Similarly, a method for tagging the NLS peptide to the DNA template can be expected[25]. However, dsDNA and NLS tagging did not increase nucleus localization[26], but there was no report on the efficiency of NLS tagged ssODN and SSTR. In this study, I found that using NLS-tagged ssODN improved the efficiency of NHEJ and SSTR. As such, NLS tagging could be a useful method since the simultaneous application of nocodazole and NLS-tagged ssODN showed a 4-fold increase in efficiency compared to nocodazole alone. Furthermore, NLS-tagged ssODN also enhanced NHEJ efficiency. Although the reason for

the increase in NHEJ frequency with NLS-tagged ssODN is unclear, NLS peptides may influence NPC activity, resulting in an increased transport of RNP to the target.

When it is not possible to utilize mitosis phase synchronization, DNA template delivery via NPC is important. For example, HR is predominant in the G2/S phase. The cells in this phase have an intact nucleus envelope, and a high HR efficiency can be achieved when energy-dependent NPC transportation is carried out via linking RNP with a DNA template[27]. Similarly, high SSTR efficiency has been induced by covalently binding RNP and ssODN[28, 29]. Direct microinjection into PN or electroporation is widely used to generate genetically engineered animals using CRISPR. In order to achieve a highly efficient HDR, the donor template should be sent to the target site prior to the nuclease. Although this is not a problem in conventional PN microinjection, other methods need to be considered for HDR mice generation, such as electroporation or microinjection into the cytoplasm. Similarly, *in vivo* HDR gene editing with adeno associated virus (AAV) is not a problem as AAV transduces into the nucleus and synthesizes Cas9 protein after dsDNA formation[30]. However, when using a non-viral vector, such as LNP, the nucleus membrane should be efficiently controlled. Recently, several studies have improved transnuclear DNA transport using supramolecules with acidity-accelerative decomposition or the NLS tagging strategy[25, 31].

In this study, I analyzed the relationship between the nuclear envelope and SSTR using embryos and cells. Recently, methods including peptide and oligo conjugation have been proposed[32], and their applicability is expected to increase, including their use in *in vivo* gene editing. In summary, HDR efficiency is determined by the DSB potential of Cas9 and the simultaneous access of the donor template. For this, it is necessary to consider a strategy based on the stages of the cell cycle and the delivery of the donor template efficiently into the nucleus. In this experiment, NLS and donor template tagging resulted in a highly efficient SSTR, a strategy that can also be applied for HDR formation, including in cells and embryos.

Chapter II

**Novel severe hemophilia A mouse
model with Factor VIII intron 22
inversion**

1. Introduction

Hemophilia A (HA) is an X-linked recessive blood coagulation disorder caused by mutations in the Factor VIII gene (*FVIII*) [33]. The estimated incidence of HA is 1:5000 males. Inversions, large deletions, nonsense and missense mutations of the *FVIII* gene can cause HA [34]. HA is classified into mild, moderate, and severe types depending on the blood coagulation factor activity. Approximately 45% of severe HA cases are caused by inversion of *FVIII* intron 22 (*FVIII* inv22) [35]. *FVIII* inv22 occurs spontaneously by non-allelic meiotic recombination between *FVIII* intron 22 and either of two inversely oriented homology regions, located by ~500 kb and 600 kb away, respectively [36].

At present, the ideal treatment for severe HA is the prophylaxis method during which coagulation factor is maintained at a concentration of 1% or more by intravenous *FVIII* infusion [37]. Despite the efficacy of protein-based therapy in HA, it presents several limitations, including short half-life of the protein, potential anti-FVIII antibodies in the patient serum, and high cost [38, 39]. Alternatively, gene therapy using non-replicating and less-integrating adeno-associated virus (AAV) has shown long-term therapeutic effect [40]. However, the exogenous DNA sequences remain in the body, and gene therapy still has the limitation of transient expression requiring repeated administration. To assess efficacy and toxicity of gene therapy, a variety of model animals have been used though all contained partial or complete deletion of *FVIII* [41].

Although gene therapy using AAV has been the most widely studied, gene correction can be used as a fundamental therapy as compared to gene therapy by changing mutations to normal gene [42]. Ultimately, a complete cure may be possible using gene correction for hematopoietic stem cells [43]. To develop this treatment for severe HA, an appropriate animal model is needed to test gene correction of *FVIII* inv22, but *FVIII* inv22 mice have not been developed yet. Currently, Clustered Regularly Interspaced Short Palindromic Repeats (CRISPR)/CRISPR associated protein (Cas9) is widely used to generate mutant mice [44]. In this study, I generated *FVIII* inv22 mice with an inversion similar to that in human HA patients using CRISPR and analyzed their hemophilia phenotype.

2. Materials and Method

2.1 sgRNA preparation

Streptococcus pyogenes Cas9 (SpCas9) was used to induce dual DNA breakage. Ten single guide RNAs (sgRNAs) were designed using an RNA guided engineered nuclease (RGEN) online tool (www.rgenome.net) on the *FVIII* intron22 and the intragenic region 319 kb away in direction of the telomere. To assess cleavage potential of sgRNA, each sgRNA and Cas9 protein were transfected into NIH3T3 cells by using a Neon electroporator (Thermo Fisher Scientific, Waltham, MA, USA). The cells were harvested after 48 h incubation, DNA was extracted, and deep sequencing was conducted on PCR amplicons using MiSeq (Illumina, San Diego, CA, USA). The indel ratio of the amplified target region was analyzed by online Cas-Analyzer (www.rgenome.net) [12]. An indel appearing 3 bp upstream of the '5-NGG-3' PAM was considered as a mutation caused by ribonucleoprotein and the indel efficiency was calculated by comparing the read sequence and reference sequence. Finally, high efficiency sgRNAs were selected and applied to animal production.

2.2 Mutant generation

C57BL/6 mice were obtained from Koatech (PyeongTaek, Korea). For estrus synchronization and superovulation, pregnant females were injected with 5 IU of serum gonadotropin (Prospec Bio, East Brunswick, USA) and 5 IU of human chorionic gonadotropin (hCG) (Prospec) at 48 h intervals. The females were then mated with the sperm donor mice. After collecting embryos from the oviduct, embryos were washed 3 times with Opti MEM I medium (Invitrogen, Carlsbad, CA, USA). Then, approximately 50 embryos were transferred into the electroporation buffer on the electrode. The final concentration of the electroporation buffer consisted of 200 ng/ μ L of SpCas9 protein (Toolgen Inc, Seoul, Korea) and 50 ng/ μ L of each sgRNA. The electroporation pulse conditions were as follows: 7 cycles of 30 V with 3 ms ON and 97 ms OFF. After washing with M2 medium (MTI-GlobalStem, Rockville, MD, USA), the embryos were transferred into the oviduct of the recipient female. Genotyping was conducted using DNA from toe-clips, and PCR and Sanger sequencing-based genotyping was conducted. This study was approved by the Institutional

Animal Care and Use Committees of Seoul National University (SNU-160721-2 and 170522-1) and was conducted in accordance with approved guidelines.

2.3 ELISA and chromogenic assay

Mouse FVIII protein concentrations in blood were measured by an enzyme-linked immunosorbent assay (ELISA) using Mouse Factor VIII ELISA kit (Mybiosource, CA, USA). Whole blood was collected in 10% sodium citrate, and plasma was freshly separated by centrifugation at 3000 rpm for 10 min at 4 °C. ELISA was according to the manufacturer's instructions. Next, concentrations of activated FVIII (FVIIIa) protein were measured using a Factor VIIIa activity assay kit (Abcam, Cambridge, UK). Fluorescent intensity (excitation / emission = 360 / 450 nm) was measured by Cytation 5 (BioTek, VT, USA). Concentrations of FVIIIa were calculated by applying the measured fluorescent intensity values to the standard curve values.

2.4 Histological examination

Mouse organs such as liver, spleen, lung, kidney and femur joint were collected, and fixed with 10% neutral formalin, and were used for hematoxylin and eosin (H&E) staining. For H&E staining, deparaffinized tissues were stained by 0.1% Mayer's H&E solution. Pathological evaluation was conducted by comparison between FVIII inv22 and wild mice under microscope.

2.5 In vivo bleeding test

To study clotting changes caused by FVIII mutation, an *in vivo* bleeding test was conducted by measuring blood loss from the distal tail vein as previously reported [45]. Briefly, mice were anesthetized via intra-peritoneal (IP) injection of avertin and, 1 cm from the distal tail was cut. Blood was collected for 20 minutes and weight of blood was normalized with body weight of the mouse (mg/g). To determine an accurate measure of blood volume, erythrocytes were separated by centrifugation at 3,000 rpm for 10 min at RT. The supernatant was removed by a vacuum pump. Erythrocytes were re-suspended in 2 mL of RBC lysis buffer and were centrifuged at 10,000 rpm for 5 min at RT. The supernatant was moved to a 96-well plate gently. Absorbance of hemoglobin was measured by a microplate spectrophotometer at 550 nm [46]. Clotting disorder was confirmed by comparison between

the normal and hemophilia phenotype.

2.6 *Survival rate analysis*

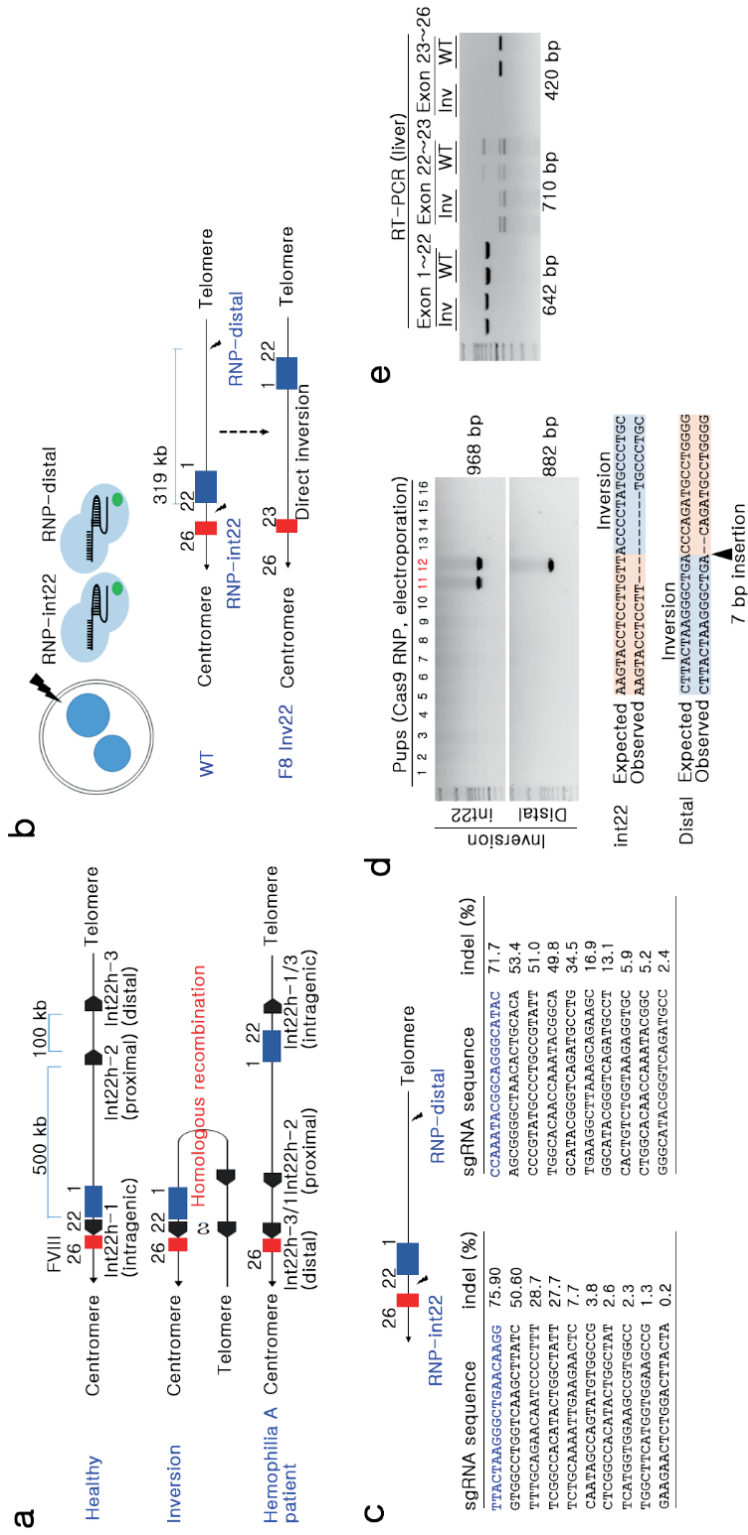
Survival rate was analyzed in 8-16-week-old male C57B6 wild type (n=13) and *FVIII* inv22 mice (n=21) over 12 days. Bleeding was induced by toe clipping on the first day of the test. After toe clipping, excessive blood loss was prevented by electrosurgical hemostasis with Change-A-Tip cautery DEL1 (Bovie medical, FL, USA). Mice were monitored daily for vital condition every. The Kaplan-Meier method was used to analyze survival rates.

3. Result

3.1 Generation of FVIII intron22 inversion mouse model

Various hemophilia models have been developed through spontaneous and targeted mutations, but inversion-based hemophilia A models have not yet been developed [41]. Human *FVIII* inversion occurs in intron 1 or intron22, but since inv22 is a major cause of severe HA [36], I attempted to develop an inv22 mouse model. Inversion mice were produced using fertilized eggs in consideration of the fact that large deletions, duplications and inversions occur in cells when dual cutting is induced using endonuclease [47]. Human inv22 occurs by homologous recombination from intron22 homolog (int22h-1) and int22h-2 and int22h-3 at a distance of 500 kb – 600 kb (Figure 6a) [48]. However, because mice do not have complete homology to the human gene sequence, one sgRNA was designed at the 22nd *FVIII* intron and the other was designed 319 kb away from the first sgRNA in the direction of the telomere (Figure 6b).

Simultaneous double strand DNA breakage (DSB) in the target site is essential for creating an inversion. Additionally, highly efficient sgRNA is critical; thus, I selected candidate sgRNAs after screening in the mouse NIH3T3 cell line (Figure 6c). Using the ribonucleoprotein (RNP) and electroporation method, 2 out of 16 mouse pups showed the *FVIII* inv22 in PCR genotyping (2/16, 12.5%). One pup appeared to have breakage of DNA fragments during the inversion (mouse No. 11), while another contained the intact form of *FVIII* inv22 (mouse No. 12, founder) after sequencing (Figure 6d). The *FVIII* inv22 was confirmed with germ line transmission by breeding *FVIII* inv22 mice with wild type mice. Mutant mice produced from this cross were used for further phenotypic analysis of hemophilia symptoms.



deep sequencing. **d)** PCR and sequencing based genotyping. **e)** RT-PCR using liver tissues for *FVIII* gene for exon 1-22, exon 22-23 and 23-26.

3.2 Validation of *FVIII* intron22 inversion-mediated blood coagulation disorder

Human *FVIII* inv22 (*hFVIII* inv22) patients form truncated *FVIII* mRNA, which results in the production of non-secreted polypeptides [45]. *mFVIII* inv22 express normal mRNA transcript from exons 1-22, but mRNA between exons 23-26 was not detected (Figure 6e). In analyzing the FVIII protein synthesis using ELISA which recognizes the FVIII exon 17 and A3 domain, *mFVIII* inv22 presented about 10% decrease in FVIII protein production, but this was not statistically significant (Figure 7b). In *mFVIII* inv22, mRNA and protein synthesis occur front of the inversion site, which is consistent with that in *hFVIII* inv22. *hFVIII* inv22 causes severe hemophilia due to the loss of part of the C1 and C2 domains, as well as no activation and secretion of the FVIII peptide (Figure 7a) [49]. Thus, a chromogenic assay was performed to assess FVIII activity. Interestingly, *mFVIII* inv22 did not exhibit FVIII activity (Figure 7b).

FVIII inv22 mice showed intermittent subcutaneous bleeding after weaning (figure 7c), but there were few dead pups before weaning. The reason for this is uncertain, but it may be due to milk fat globule-epidermal growth factor 8 (MFG-E8) protein from mother mouse, which has a similar sequence to that of FVIII protein [50]. Therefore, the hemophilia phenotype analysis was performed on animals of 7 weeks of age or older. Histopathological analysis revealed that *mFVIII* inv22 developed extramedullary hematopoiesis (EMH) in the spleen (figure 7d). EMH is remnants of fetal blood production and are mainly found in thrombocytopenia, myelofibrosis or thalassemia [51, 52]. EMH occurs mainly in abnormalities of hematopoiesis and has not yet been reported in human hemophilia. An additional *in vivo* bleeding assay exhibited severe hemophilic disorder in *mFVIII* inv22 mice, as evidenced by extended bleeding time and high blood loss. Since the *in vivo* bleeding experiment lasted only 20 minutes, the amount of blood loss in *mFVIII* inv22 mice was doubled (Figure 7e). When bleeding was induced in mice older than 7 weeks, wild type mice survived for 12 weeks, but *mFVIII* inv22 mice showed more than 50% of death rate in 9 weeks (Figure 7f). In summary, *mFVIII* inv22 mice developed a clotting disorder, severe hemophilia, and high mortality.

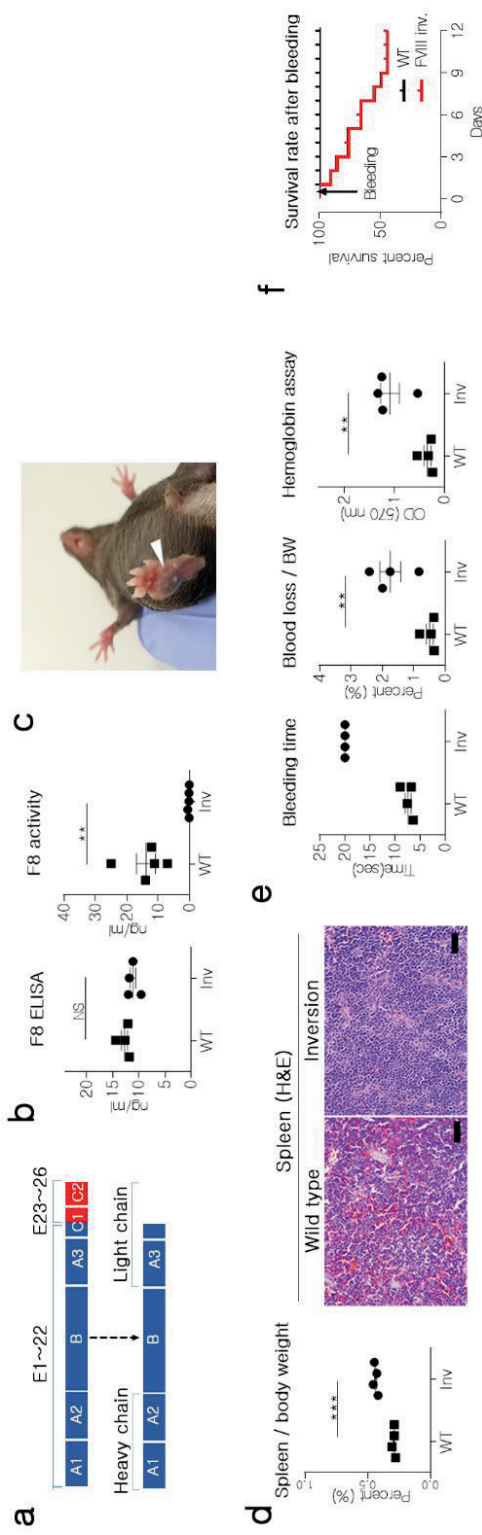


Figure 7. Hemophilia phenotyping with *FVIII* inv22 mice. **a**) Brief map of expected *FVIII* domain of *FVIII* inv22 mice. **b**) Analysis for circulating *FVIII* protein and its activity. Each dot indicates data from an individual mouse. **c**) Subcutaneous bleeding in *FVIII* inv22 mice. **d**) Enlarged spleen in *FVIII* inv22 mice and histological analysis. Black bar: 50 μ m. *** indicates $p < 0.001$. **e**) Clotting activity was evaluated with *in vivo* bleeding test. Bleeding time and blood loss was calculated and compared between *FVIII* inv22 and wild type mice. ** indicates $p < 0.01$. **f**) Survival rate was analyzed after intended bleeding and hemostasis (Wild; n=13, *FVIII* inv22; n = 21).

4. Discussion

Various types of HA animal models have been developed, and *FVIII* exon 16 and 17 targeting or total gene deletion models have been reported [45, 53]. *FVIII* inv22 mice exhibited a phenotype similar to the existing animal model, with little FVIII activity. However, while previous models focused on deficiency of FVIII protein, the newly developed *FVIII* inv22 mouse was focused on structural variation that causes severe HA. *FVIII* inv22 mice showed severe hemophilia symptoms, but unlike humans, they presented EMH and circulating FVIII protein [54]. These circulating mutant FVIII protein would influence inhibitor risk [55], but I did not analyze *FVIII*-cross-reactive material issue with *FVIII* inv22 mice.

Currently, hemophilia A research is being conducted in various animal species such as mice, dogs, sheep and pigs [41]. In humans, clinical trials using AAV are ongoing and the effects of AAV-mediated gene therapy lasted approximately one year [56]. However, there are several limitations of AAV-mediated gene therapy; the gradual decrease in therapeutic efficacy, high frequencies of anti-AAV antibody response in human and difficult to control the therapeutic effects [57]. For this reason, AAV-mediated gene therapy is not suitable complete therapy for hemophilia A. Therefore, gene correction technology is needed to permanent therapy for genetic disorder including hemophilia A in future.

I developed novel *FVIII* inv22 mice using CRISPR/Cas9 system. However, due to the genetic difference between humans and mice, further analysis is needed for confirmation of its validity. As a hemophilia model due to genetic mutations and loss of FVIII activity the *FVIII* inv22 mice developed are similar to other conventional mouse models. However, it may be a useful model for studying the fundamental mechanism of severe hemophilia that occurs in human patients with *FVIII* inv22 or to study new therapeutic approaches. Gene therapy is the trend in recent hemophilia research. I think that our *FVIII* inv22 mouse could be a model for further disease cure through endogenous gene correction. In addition, various types of genetic disease caused by structural variation have been reported in human [58]. By applying the dual DSB breakage method applied in this study, another structural variant human disease animal model could be established.

References

1. Jinek, M., et al., *A programmable dual-RNA-guided DNA endonuclease in adaptive bacterial immunity*. Science, 2012. **337**(6096): p. 816-21.
2. Richardson, C.D., et al., *CRISPR-Cas9 genome editing in human cells occurs via the Fanconi anemia pathway*. Nat Genet, 2018. **50**(8): p. 1132-1139.
3. Renaud, J.B., et al., *Improved Genome Editing Efficiency and Flexibility Using Modified Oligonucleotides with TALEN and CRISPR-Cas9 Nucleases*. Cell Rep, 2016. **14**(9): p. 2263-72.
4. Bertoni, C., A. Rustagi, and T.A. Rando, *Enhanced gene repair mediated by methyl-CpG-modified single-stranded oligonucleotides*. Nucleic Acids Res, 2009. **37**(22): p. 7468-82.
5. Riesenberger, S. and T. Maricic, *Targeting repair pathways with small molecules increases precise genome editing in pluripotent stem cells*. Nat Commun, 2018. **9**(1): p. 2164.
6. Jang, D.E., et al., *Multiple sgRNAs with overlapping sequences enhance CRISPR/Cas9-mediated knock-in efficiency*. Exp Mol Med, 2018. **50**(4): p. 16.
7. Rothkamm, K., et al., *Pathways of DNA double-strand break repair during the mammalian cell cycle*. Mol Cell Biol, 2003. **23**(16): p. 5706-15.
8. Arnoult, N., et al., *Regulation of DNA repair pathway choice in S and G2 phases by the NHEJ inhibitor CYREN*. Nature, 2017. **549**(7673): p. 548-552.
9. Lin, S., et al., *Enhanced homology-directed human genome engineering by controlled timing of CRISPR/Cas9 delivery*. Elife, 2014. **3**: p. e04766.
10. Yang, D., et al., *Enrichment of G2/M cell cycle phase in human pluripotent stem cells enhances HDR-mediated gene repair with customizable endonucleases*. Sci Rep, 2016. **6**: p. 21264.
11. Hashimoto, M., Y. Yamashita, and T. Takemoto, *Electroporation of Cas9 protein/sgRNA into early pronuclear zygotes generates non-mosaic mutants in the mouse*. Dev Biol, 2016. **418**(1): p. 1-9.
12. Park, J., et al., *Cas-analyzer: an online tool for assessing genome editing results using NGS data*. Bioinformatics, 2016.
13. Chazaud, C. and Y. Yamanaka, *Lineage specification in the mouse preimplantation embryo*. Development, 2016. **143**(7): p. 1063-74.
14. Kim, J., et al., *Maternal Setdb1 Is Required for Meiotic Progression and Preimplantation Development in Mouse*. PLoS Genet, 2016. **12**(4): p. e1005970.
15. Wossidlo, M., et al., *5-Hydroxymethylcytosine in the mammalian zygote is linked with epigenetic reprogramming*. Nat Commun, 2011. **2**: p. 241.
16. Kang, E., et al., *Nuclear reprogramming by interphase cytoplasm of two-cell mouse embryos*. Nature, 2014. **509**(7498): p. 101-4.
17. Signorello, E., et al., *Nocodazole Induced Suicidal Death of Human Erythrocytes*. Cell Physiol Biochem, 2016. **38**(1): p. 379-92.
18. Salman, H., et al., *Kinetics and mechanism of DNA uptake into the cell nucleus*. Proc Natl Acad Sci U S A, 2001. **98**(13): p. 7247-52.
19. Zhang, J.P., et al., *Efficient precise knockin with a double cut HDR donor after CRISPR/Cas9-mediated double-stranded DNA cleavage*. Genome Biol, 2017. **18**(1):

- p. 35.
20. Gavet, O. and J. Pines, *Activation of cyclin B1-Cdk1 synchronizes events in the nucleus and the cytoplasm at mitosis*. J Cell Biol, 2010. **189**(2): p. 247-59.
21. Adli, M., *The CRISPR tool kit for genome editing and beyond*. Nat Commun, 2018. **9**(1): p. 1911.
22. Rodriguez, A. and A. D'Andrea, *Fanconi anemia pathway*. Curr Biol, 2017. **27**(18): p. R986-R988.
23. Nalepa, G. and D.W. Clapp, *Fanconi anemia and the cell cycle: new perspectives on aneuploidy*. F1000Prime Rep, 2014. **6**: p. 23.
24. Kee, Y., J.M. Kim, and A.D. D'Andrea, *Regulated degradation of FANCM in the Fanconi anemia pathway during mitosis*. Genes Dev, 2009. **23**(5): p. 555-60.
25. Giraud, G., et al., *NLS-tagging: an alternative strategy to tag nuclear proteins*. Nucleic Acids Res, 2014. **42**(21).
26. Tanimoto, M., et al., *No enhancement of nuclear entry by direct conjugation of a nuclear localization signal peptide to linearized DNA*. Bioconjug Chem, 2003. **14**(6): p. 1197-202.
27. Gu, B., E. Posfai, and J. Rossant, *Efficient generation of targeted large insertions by microinjection into two-cell-stage mouse embryos*. Nat Biotechnol, 2018. **36**(7): p. 632-637.
28. Aird, E.J., et al., *Increasing Cas9-mediated homology-directed repair efficiency through covalent tethering of DNA repair template*. Commun Biol, 2018. **1**: p. 54.
29. Savic, N., et al., *Covalent linkage of the DNA repair template to the CRISPR-Cas9 nuclease enhances homology-directed repair*. Elife, 2018. **7**.
30. Wang, D., P.W.L. Tai, and G. Gao, *Adeno-associated virus vector as a platform for gene therapy delivery*. Nat Rev Drug Discov, 2019.
31. Zhu, J.Y., et al., *Propelled Transnuclear Gene Transport Achieved through Intracellularly Redox-Responsive and Acidity-Accelerative Decomposition of Supramolecular Fluorescence-Quenchable Vectors*. ACS Appl Mater Interfaces, 2017. **9**(1): p. 255-265.
32. Lou, C., et al., *Peptide-oligonucleotide conjugates as nanoscale building blocks for assembly of an artificial three-helix protein mimic*. Nat Commun, 2016. **7**: p. 12294.
33. Bowen, D.J., *Haemophilia A and haemophilia B: molecular insights*. Mol Pathol, 2002. **55**(2): p. 127-44.
34. Gouw, S.C., et al., *F8 gene mutation type and inhibitor development in patients with severe hemophilia A: systematic review and meta-analysis*. Blood, 2012. **119**(12): p. 2922-34.
35. Johnsen, J.M., et al., *Novel approach to genetic analysis and results in 3000 hemophilia patients enrolled in the My Life, Our Future initiative*. Blood Adv, 2017. **1**(13): p. 824-834.
36. Dutta, D., et al., *Accurate, simple, and inexpensive assays to diagnose F8 gene inversion mutations in hemophilia A patients and carriers*. Blood Adv, 2016. **1**(3): p. 231-239.
37. Srivastava, A., et al., *Guidelines for the management of hemophilia*. Haemophilia, 2013. **19**(1): p. e1-47.
38. Evatt, B.L. and L. Robillard, *Establishing haemophilia care in developing countries: using data to overcome the barrier of pessimism*. Haemophilia, 2000. **6**(3): p. 131-4.
39. Gouw, S.C., et al., *Influence of the type of F8 gene mutation on inhibitor development in a single centre cohort of severe haemophilia A patients*.

- Haemophilia, 2011. **17**(2): p. 275-81.
40. Dunbar, C.E., et al., *Gene therapy comes of age*. Science, 2018. **359**(6372).
41. Yen, C.T., et al., *Current animal models of hemophilia: the state of the art*. Thromb J, 2016. **14**(Suppl 1): p. 22.
42. Maeder, M.L. and C.A. Gersbach, *Genome-editing Technologies for Gene and Cell Therapy*. Mol Ther, 2016. **24**(3): p. 430-46.
43. Pavel-Dinu, M., et al., *Gene correction for SCID-X1 in long-term hematopoietic stem cells*. Nat Commun, 2019. **10**(1): p. 1634.
44. Wang, H., et al., *One-step generation of mice carrying mutations in multiple genes by CRISPR/Cas-mediated genome engineering*. Cell, 2013. **153**(4): p. 910-8.
45. Chao, B.N., et al., *Characterization of a genetically engineered mouse model of hemophilia A with complete deletion of the F8 gene*. J Thromb Haemost, 2016. **14**(2): p. 346-55.
46. Liu, Y., et al., *Standardizing a simpler, more sensitive and accurate tail bleeding assay in mice*. World J Exp Med, 2012. **2**(2): p. 30-6.
47. Lee, H.J., et al., *Targeted chromosomal duplications and inversions in the human genome using zinc finger nucleases*. Genome Res, 2012. **22**(3): p. 539-48.
48. Bowen, D.J., *Haemophilia A and haemophilia B: molecular insights*. Mol Pathol, 2002. **55**(1): p. 1-18.
49. Pandey, G.S., et al., *Endogenous factor VIII synthesis from the intron 22-inverted F8 locus may modulate the immunogenicity of replacement therapy for hemophilia A*. Nat Med, 2013. **19**(10): p. 1318-24.
50. Yi, Y.S., *Functional Role of Milk Fat Globule-Epidermal Growth Factor VIII in Macrophage-Mediated Inflammatory Responses and Inflammatory/Autoimmune Diseases*. Mediators Inflamm, 2016. **2016**: p. 5628486.
51. Zaninetti, C., et al., *Extramedullary hematopoiesis: a new feature of inherited thrombocytopenias?* J Thromb Haemost, 2017. **15**(11): p. 2226-2229.
52. Chunduri, S., et al., *Pulmonary extramedullary hematopoiesis in patients with myelofibrosis undergoing allogeneic stem cell transplantation*. Haematologica, 2008. **93**(10): p. 1593-5.
53. Sarkar, R., et al., *Partial correction of murine hemophilia A with neo-antigenic murine factor VIII*. Hum Gene Ther, 2000. **11**(6): p. 881-94.
54. Oldenburg, J. and A. Pavlova, *Genetic risk factors for inhibitors to factors VIII and IX*. Haemophilia, 2006. **12 Suppl 6**: p. 15-22.
55. Sauna, Z.E., et al., *The intron-22-inverted F8 locus permits factor VIII synthesis: explanation for low inhibitor risk and a role for pharmacogenomics*. Blood, 2015. **125**(2): p. 223-8.
56. Rangarajan, S., et al., *AAV5-Factor VIII Gene Transfer in Severe Hemophilia A*. N Engl J Med, 2017. **377**(26): p. 2519-2530.
57. Calcedo, R. and J.M. Wilson, *Humoral Immune Response to AAV*. Front Immunol, 2013. **4**: p. 341.
58. Puig, M., et al., *Human inversions and their functional consequences*. Brief Funct Genomics, 2015. **14**(5): p. 369-79.

;

국문초록

CRISPR/Cas 시스템은 유전체 편집에 널리 사용되고 있다. 이 시스템은 진핵세포에서 오류가 발생하기 쉬운 NHEJ와 오류가 없는 HDR을 일으키는데, 이를 이용해 편집을 하게 된다. 유전체 편집 분야에서 녹인 (KI) 효율을 높이는 것은 굉장히 중요한 문제여서, 나는 효율을 높이는 메커니즘에 대해 연구했다. 또한, 현재까지 혈우병 A 유전자 역위 마우스 모델이 존재하지 않기 때문에 CRISPR/Cas9 시스템을 이용해 새로운 유전자 역위-매개 혈우병 A 마우스 모델을 생산하였다.

녹인 효율을 높이기 위해서 단일 가닥 올리고 뉴클레오타이드 (ssODN)를 주형으로 사용하였고, 전기 천공에 의한 녹인 효율을 평가하기 위해 세포 주기에 따라 면역 염색을 통해서 RNP 복합체와 ssODN의 이동을 관찰하였다. 유사 분열기, 특히 중기 및 후기가 핵막이 없는 상태로 최적의 SSTR 효율을 보이는 것을 확인하였다. NLS를 갖는 Cas9 단백질은 핵 안으로 쉽게 이동하지만, ssODN은 유사 분열기 전에는 핵막에 막혀 핵 안으로 들어가지 않았다. 이 때문에 ssODN이 핵 안에 도착하기 전에 이미 NHEJ가 발생한다. 핵막 때문에 생기는 문제를 피하기 위해서 NLS를 태깅한 ssODN을 실험에 사용하였다. NLS를 태깅한 그룹은 대조군보다 4배 이상 향상된 SSTR 효율을 나타냈다. 요약하면, CRISPR/Cas를 통한 유전체 편집에서 녹인 효율을 최대화하기 위해서는 유사 분열 단계에서 실험을 수행하거나 NLS를 태깅한 ssODN을 주형 템플릿으로 사용해야 한다.

CRISPR/Cas의 발견은 유전자 편집 동물 모델을 생산하는 새로운 시대의 출발점이다. 수많은 새로운 동물 모델이 생산되었지만, FVIII intron22 역위 중증 혈우병 A 마우스 모델에 대한 선행 연구가 아직까지 존재하지 않는다. 사람에서의 중증 혈우병 A를 모방하기 위해 나는 마우스 배아에서 CRISPR/Cas 시스템을 이용해 NHEJ-매개 FVIII inv22를 유도하였다. 이렇게 생산된 FVIII inv22 마우스는 FVIII의 활성도가 극히 낮아졌고, 혈액 응고 장애 및 높은 사망률 등의 혈우병 표현형을 나타냈다.

결론적으로 나의 연구결과는 유사 분열기가 SSTR의 최적의 단계이고 주형 템플릿은 nuclease 이전에 핵 안으로 전달되어야 한다는 것을 밝혀냈다. 추가적으로, 혈우병 A의 유전자 치료 및 유전자 교정 연구에 적합한 전임상 마우스 모델을 생산하였다.

감사의 글

대학을 졸업한 이후에도 2년 간의 학위 과정 동안, 저를 믿어 주시고 모든 방
면에서 지원해주신 제 아버지, 어머니께 감사드립니다. 그리고 대학원에서의 학
업과 생활에 많은 도움과 조언을 주신 염수청 교수님께 감사드립니다.